

1.8 m/0.5 s Resolution Coherent Doppler Wind Lidar Using Continuous Phase Modulation

Yunpeng Zhang , Yunbin Wu, Jingjing Dong, and Haiyun Xia 

Abstract—A high-spatial-resolution coherent Doppler wind lidar (CDWL) with high modulation efficiency is reported. The pseudo-random phase coding (PRPC) links the spatial resolution to the modulation rate but suffers from the non-rectangular transition states caused by the limited bandwidth. With the help of continuous phase modulation (CPM), the abrupt phase switching between successive bit intervals is avoided, thus significantly reducing the bandwidth requirement. By mapping the binary sequence into different transition states rather than phase levels, a 10-fold modulation efficiency improvement is realized. In experiments, the performance of the proposed lidar is compared with lidars in the PRPC method and conventional non-coding method. Continuous radial wind profile measurement of 800 m is demonstrated with spatial and temporal resolution of 1.8 m and 0.5 s, which is the highest spatial resolution realized by a pulsed CDWL to our best knowledge.

Index Terms—Coherent doppler lidar, continuous phase modulation, spatial resolution.

I. INTRODUCTION

THE remote sensing of wind velocity by the Doppler frequency shift is an established technique. Under this principle, the Doppler wind lidar is a quite promising candidate with advantages including large scan volume, movability, provision of 3-dimensional wind measurements and relatively high temporal and spatial resolution [1]. It has been widely used in scientific research and engineering applications, such as gravity waves monitoring [2], [3], boundary layer detection [4], [5], wind resource assessment [6], [7], weather forecast [8], [9], and air pollution analysis [10], [11]. Boosted by the development of coherent detection, a coherent Doppler wind lidar (CDWL) further provides the range resolved atmospheric backscattered

spectra, promoting the Doppler lidar towards versatility. Besides wind profiling, spectrum analysis based applications of the CDWLs like precipitation observation [12], [13] and cloud phase identification [14] have been reported.

Among all the applications, areas like aviation safety [15], [16] and turbulence detection [17], [18] raise higher requirements on spatial resolution. Typically, the wingspan of the aircraft is on the order of ten meters, meter-scale detection of the wind field can be beneficial for the wake vortex parameters estimation [19], [20]. In atmospheric boundary layer turbulence detection, the fine wind profiles are usually got by the radiosonde [21]. Though a quite high spatial resolution can be realized by the continuous wave lidar [22], [23], [24], it's still not comparable with the pulsed CDWL in aspect of wide-range wind profiling. The high-spatial-resolution CDWL is expected to provide a high-efficiency and low-cost remote sensing approach besides the in-situ measurement.

Recently, several methods are reported to enhance the spatial resolution of the pulsed CDWL to sub 5 meters [25], [26], [27]. In the differential correlation pair (DCP) method [25], pulses composed of a common pulse and a probing pulse are employed in pair while the spatial resolution is determined by the duration of the short probing pulse. To further increase the spatial resolution, it could be challenging to amplify a short probing pulse without distortion at high power. Meanwhile, the pseudo-random phase coding (PRPC) method [27] decouples the spatial resolution and pulse duration by the pseudo-random phase modulation. Thus, the high spatial resolution can be realized without shortening the pulse amplitude envelope. However, a very high modulation bandwidth is required to support the fast phase transition between modulation bits. Under a specific bandwidth, the non-instantaneous transition with rising and falling edges would hinder the improvement of spatial resolution [27].

In this work, we propose a novel method incorporating pseudo-random continuous phase modulation (PR-CPM) to avoid the mentioned high bandwidth requirement. Considering that the analog bandwidth is mainly increased by the abrupt phase switching [28], a significant modulation efficiency improvement can be achieved by mapping the pseudo-random binary sequence (PRBS) into different transition states rather than phase levels. In demodulation, the digital interferometry [29] and spectrum difference [27] technique are employed to extract the distributed backscattered signals with different time delay and reconstruct the range resolved spectra. In Section II, the principle of the PR-CPM lidar is illustrated by theoretical

Manuscript received 22 July 2022; revised 17 August 2022; accepted 20 August 2022. Date of publication 23 August 2022; date of current version 31 August 2022. This work was supported in part by the National Ten Thousand Talent Program in China and in part by the Strategic Priority Research Program of Chinese Academy of Sciences under Grant XDA22040601. (Corresponding author: Haiyun Xia.)

Yunpeng Zhang and Yunbin Wu are with the School of Earth and Space Sciences, University of Science and Technology of China, Hefei 230026, China (e-mail: zyp110@mail.ustc.edu.cn; wuyunbin@mail.ustc.edu.cn).

Jingjing Dong is with the School of Atmospheric Physics, Nanjing University of Information Science and Technology, Nanjing 210044, China (e-mail: 850444@nuist.edu.cn).

Haiyun Xia is with the School of Earth and Space Sciences, USTC, Hefei 230026, China, with the School of Atmospheric Physics, Nanjing University of Information Science and Technology, Nanjing 210044, China, with the Hefei National Laboratory for Physical Sciences at the Microscale, USTC, Hefei 230026, China, and also with Institute of Software, Chinese Academy of Sciences, Beijing 100190, China (e-mail: hsia@ustc.edu.cn).

Digital Object Identifier 10.1109/JPHOT.2022.3201025

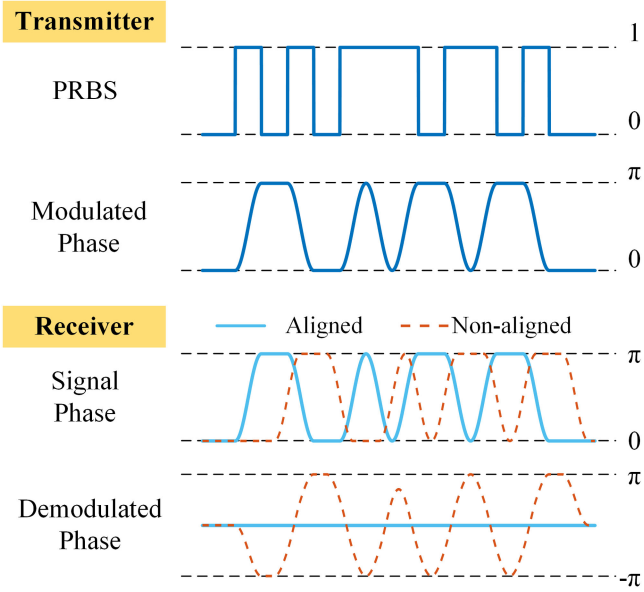


Fig. 1. Modulation and demodulation scheme of the PR-CPM lidar. The “0” and “1” are mapped to the operations of keeping the phase unchanged and smoothly reversing the phase, respectively.

analysis and simulation. Then the system setup is described in Section III. The proposed method is experimentally compared with the PRPC and conventional non-coding methods in Section IV. In experiments, the PR-CPM shows similar performance with the PRPC method at much lower bandwidth requirement. Finally, the high-resolution wind profiling at 1.8 m/0.5 s is demonstrated in a range of 800 m.

II. PRINCIPLE AND SIMULATION

The principle of the proposed PR-CPM method is illustrated in Fig. 1. In the transmitter, a PRBS is used to generate the phase signal. The “0” and “1” are mapped to the operations of keeping the phase unchanged and smoothly reversing the phase to avoid the discontinuity. Specifically, when the current bit is “0”, the phase keeps unchanged as 0 or π according to the previous phase state; when the current bit is “1”, the phase reverses in a bit interval T_b . One can design the reversing process as a raised cosine function with roll-off factor of 1 [30]. As the bits and modulated phase sequences are denoted as $b[i]$ and $\theta_i(t)$, during $(0, T_b]$, this mapping can be summarized as:

$$\theta_i(t) = \theta_{i-1}(T_b) + b[i] \cos[\theta_{i-1}(T_b)] \cdot \frac{\pi}{2} \left[1 - \cos\left(\frac{\pi t}{T_b}\right) \right], \quad (1)$$

where θ_{-1} is set to be zero as the initial condition. According to (1), the phase within the i th bit interval is listed in Table I under different conditions.

After phase modulation, the electric field of the lightwave is:

$$E(t) = A(t) \exp[j2\pi f_c t + j\theta(t)], \quad (2)$$

TABLE I
MAPPING FROM BITS TO PHASES

$b[i]$	$\theta_{i-1}(T_b)$	$\theta_i(0)$	$\theta_i(t)$
0	0	0	0
0	π	π	π
1	0	0	$\frac{\pi}{2} \left[1 - \cos\left(\frac{\pi t}{T_b}\right) \right]$
1	π	π	$\frac{\pi}{2} \left[1 + \cos\left(\frac{\pi t}{T_b}\right) \right]$

where $A(t)$ is the amplitude envelope of the unmodulated pulse, f_c is the carrier frequency, and $\theta(t) = \sum \theta_i(t - iT_b)$ is the continuous phase signal constructed by the sum of phases within each bit interval.

According to the classical layered model of atmospheric scattering [31], the backscattered signal can be modeled as the superposition of random atmospheric reflections from different slices. After heterodyne detection, the received signal is:

$$r(t) = \int A\left(t - \frac{2z}{c}\right) \kappa(z) \times \cos\left\{2\pi [f_d(z) + f_{IF}]t + \theta\left(t - \frac{2z}{c}\right)\right\} dz, \quad (3)$$

where $f_{IF} = f_c - f_{LO}$ is the intermediate frequency (IF) with f_{LO} being the frequency of the local oscillator, $f_d(z)$ is the Doppler frequency shift caused by the motion of aerosols, c is the speed of light in the atmosphere, and $\kappa(z)$ is a random variable representing the random scattering feature of the atmosphere. (3) indicates that the heterodyne signals originate from different distances share the same phase pattern but have different time delay $\tau = 2z/c$. Though the signals generated by adjacent locations partly overlap in time, they can be separated by the auto-correlation property of the pseudo-random phase $\theta(t)$.

To isolate the backscattered signal from distance $z_0 = ct_0/2$, the delayed phase signal $\theta(t - t_0)$ is used as the reference phase. As shown by the cyan-solid line and red-dash line in Fig. 1, only the signal having the same delay as the reference signal could show a constant phase after demodulation, otherwise, the phase remains random. In demodulation, the received IF signal is first truncated by a delayed window function $W(t - t_0)$ and then digitally interfered with a digital reference signal $R(t - t_0)$. Usually, the window function is set to be the same as the pulse's amplitude envelope $A(t)$. Considering that the received signal is real, the reference signal is defined as [32]:

$$R(t) = \cos[\theta(t)]. \quad (4)$$

In frequency domain, the spectra of the non-aligned signals are spread across a broad bandwidth, while the spectrum of the aligned signal is narrow [33]. Therefore, the backscattered signal around z_0 is separated with the spatial resolution of $\Delta z = cT_b/2$ [27].

To further reduce the interference introduced by the non-aligned signals, the spectrum difference technique can be used

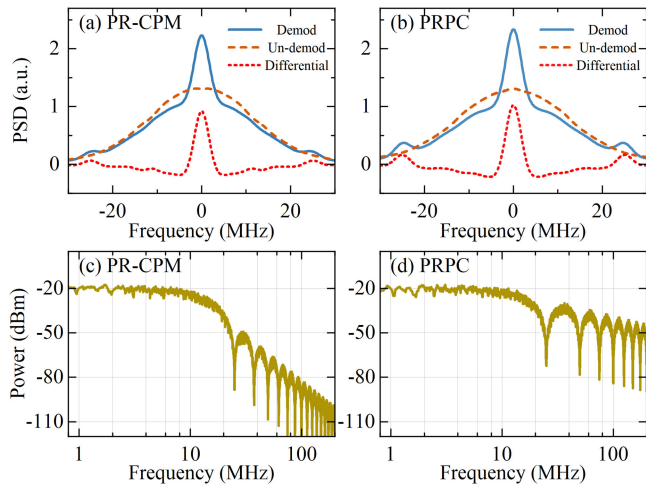


Fig. 2. Illustration of the demodulated, un-demodulated and differential spectra in (a) PR-CPM (b) PRPC method. Demod, demodulated; Un-demod, un-demodulated; and PSD, power spectral density. Spectrum of the phase signal in (c) PR-CPM (d) PRPC method.

[27]. The difference between the spectra before and after demodulation could eliminate the spectra of the non-aligned signals. To compare the spectra of the PRPC and PR-CPM methods, a numerical simulation is conducted based on (3) and (4). In both methods, the pulse shapes are set to be truncated Gaussian function with full width at half maximum (FWHM) of the amplitude envelope being 240 ns. The modulation bit interval of the PRBS is 40 ns. As shown in Fig. 2(a) and (b), the spectra of the un-demodulated signals are spread by the pseudo-random modulation. After demodulation, the spectrum of the aligned signal is despread by interfering with the reference signal while those of the non-aligned signals are still wide due to the random phase. Thus, the spread and despread portions constitute the main part of the demodulated signal's spectrum. In addition, the harmonic components corresponding to the modulation rate of $R_b = 1/T_b$ are introduced in the demodulated spectra. Since the abrupt phase transition is avoided in the PR-CPM method, the harmonic components in Fig. 2(a) are much smaller compared to those in Fig. 2(b). Though the backscattered spectra of the two methods are similar, the spectra of the phase signals in Fig. 2(c) and (d) are quite different. Note that the spectrum of the phase signal is directly linked to the bandwidth requirement of the modulation related devices. The Fig. 2 implies a much lower bandwidth requirement of the PR-CPM method under similar performance with the PRPC method.

III. SYSTEM SETUP

The system setup of the proposed PR-CPM lidar is shown in Fig. 3. In the transmitter, a continuous-wave laser (CW, Amonics ALiDAR-150-Seed) is split into two parts. The major and minor portions are used as the master oscillator (MO) of the transmitted signal and the local oscillator (LO), respectively. The MO is frequency shifted by 80 MHz and chopped into pulses with repetition rate of 10 kHz by an acousto-optic modulator (AOM). The pulses are phase modulated by an electro-optic phase modulator (EOPM, ixblue MPZ-LN-20) with the half-wave voltage

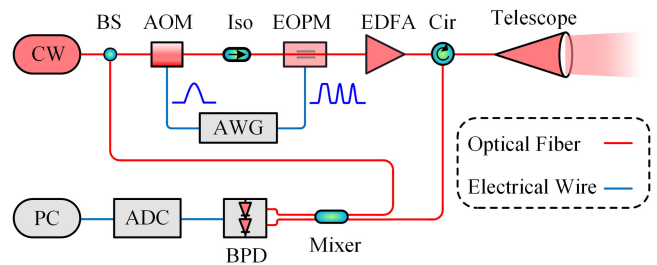


Fig. 3. System setup of the PR-CPM lidar. CW, continuous-wave laser; BS, beam splitter; Iso, isolator; AOM, acousto-optic modulator; EOPM, electro-optic phase modulator; EDFA, erbium-doped fiber amplifier; Cir, circulator; BPD, balanced photodetector; ADC, analog-to-digital converter; AWG, arbitrary waveform generator; and PC, personal computer.

TABLE II
SUMMARY OF KEY SYSTEM PARAMETERS

Parameters	Value
Transmitter:	
Center wavelength	1550 nm
Pulse peak power	350 W
Pulse repetition rate	10 kHz
AOM frequency shift	80 MHz
AOM extinction ratio	80 dB
Transceiver:	
Telescope diameter	100 mm
Focal length	550 mm
Beam full divergence	44 μ rad
Circulator isolation	30 dB
Receiver:	
LO power	1.5 mW
Receiving bandwidth	220 MHz
Sample rate	500 MSps
Temporal resolution	0.5 s

of 7 V. To generate the pseudo-random phase signal, a 12-bit M-sequence [34] is used. A high-power erbium-doped fiber amplifier (EDFA, Amonics ALiDAR-150-AMP) is employed to amplify the modulated pulses. The peak power is limited below the stimulated Brillouin scattering threshold [35] to avoid the distortion induced by the nonlinear effects.

A monostatic configuration with a 100-mm telescope is used as the transceiver. In the receiver, the backscattered optical signal is guided by a circulator to mix with the LO, and then down converted into electrical signal in IF band by beating on a balanced photodetector (BPD). To avoid frequency aliasing, the analog bandwidth of the receiver is limited to 220 MHz. After digitized by an analog-to-digital converter (ADC), the raw data are stored in a computer for further processing. The AOM, EOPM and ADC are synchronized on a common reference provided by the arbitrary waveform generator (AWG, Keysight 33622A). The key system parameters are summarized in Table II.

In data processing, a window function matched to the amplitude envelope of the pulse's electric field is used to achieve optimum receiving [36]. After demodulation, the backscattered spectra from multiple pulses are incoherently accumulated to improve the estimation accuracy of the Doppler frequency shift [37]. We set the temporal resolution as 0.5 second here, averaging the backscattered spectra of 5k pulses. For each pulse, the range resolved backscattered spectrum is obtained by the periodogram [38], where the fast Fourier transform (FFT) length

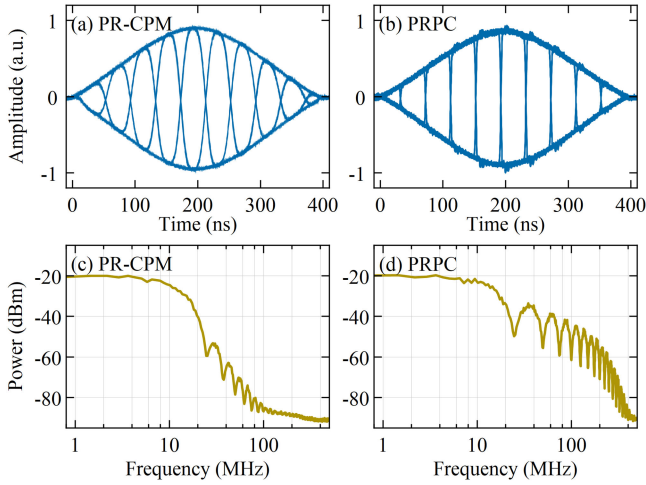


Fig. 4. Eye diagram of the modulated lightwave with $T_b = 40$ ns in (a) PR-CPM (b) PRPC method. Spectrum of the EOPM's driving signal in (c) PR-CPM (d) PRPC method.

is extended to 2048 through zero padding, corresponding to the frequency sampling interval of 0.244 MHz. The Gaussian fit is used to estimate the Doppler frequency shift from the backscattered spectrum and the wind velocity is finally derived from the estimated Doppler frequency shift.

IV. EXPERIMENT AND DISCUSSIONS

During the experiments, the system is placed on the 9th floor of the laboratory building (32.20 °N, 118.72 °E) with the telescope pointing to the south at an elevation angle of 15°. In each measurement, the continuous storage of the digitized backscattered signal can last for at most 8 seconds, limited by the size of the onboard memory.

A. Proof-of-Concept Experiment

To validate the proposed PR-CPM method, its performance is compared with a CDWL based on the PRPC method at the same spatial resolution. In both methods, the FWHM of the pulsed lightwave's envelope and the modulation bit interval are set to be 240 ns and 40 ns, respectively. For brevity, the two systems will be referred to as CPM-40 ns and PC-40 ns, according to the time parameter directly related to spatial resolution.

The modulated lightwave is first observed by homodyne detection with a 180° optical hybrid. Fig. 4(a) and (b) show the eye diagrams of the modulated signals in the two methods, which are formed by overlaying the in-phase component [39] of the pulses' electric field. In the PR-CPM method, the rising edge can last for the whole bit interval T_b , while that of the PRPC method is usually limited to no more than $0.1T_b$ to avoid the degradation of the range resolved signal. Since the bandwidth of a practical step signal is inversely proportional to its rise time [40], compared to the PRPC method, 90% modulation bandwidth is saved by the CPM. In other words, a 10-fold modulation efficiency improvement is achieved. As shown in Fig. 4(c) and (d), the power spectra of the modulating signals

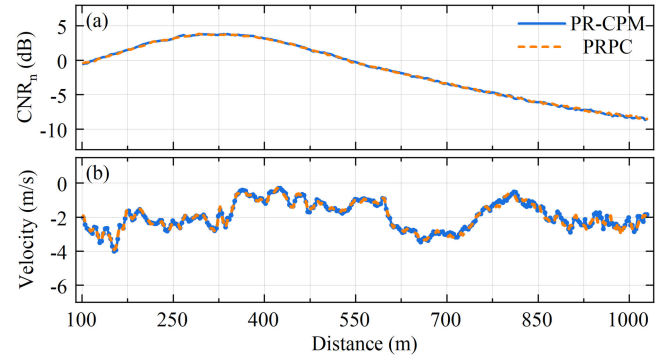


Fig. 5. (a) Narrowband CNR and (b) Radial wind velocity profiles of the PR-CPM lidar and the PRPC lidar.

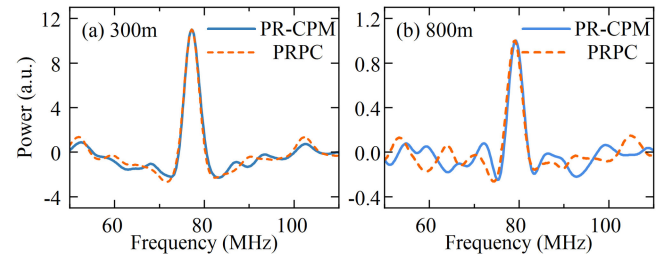


Fig. 6. Normalized spectra of the PR-CPM and PRPC lidar at (a) 300 m and (b) 800 m.

feeding to the EOPM are measured by a spectrum analyzer (R&S FSVR7) with the resolution bandwidth (RBW) being 100 kHz.

In the wind profiling, measurement results got by the two methods are plotted in Fig. 5, where the blue solid line and orange dash line stand for the CPM-40ns and PC-40ns, respectively. As shown in Fig. 5(a), the narrowband CNR [41] of the two methods are close as they share the system specification listed in Table II. In Fig. 5(b), the radial wind velocity profiles measured by the two methods are quite consistent within 800 m, confirming the PR-CPM lidar's spatial resolution. Between 800 and 1000 m, the profiles slightly fluctuate around each other due to the lower CNR.

The differential spectra of the two methods are shown in Fig. 6. At 300 m where the CNR is high, the spectra are similar with the simulation results in Fig. 2. The harmonic components in the PR-CPM method are smaller than those in PRPC method. In both methods, the spectrum broadening is avoided as the width of the main spectral peak is determined by the pulse envelope rather than modulation rate [27], which is beneficial to the estimation accuracy of the Doppler frequency shift [42]. At low CNR region shown in Fig. 6(b), though the differential spectra deviate from the ideal shapes due to the noise, the signal peaks can still be discriminated from the noise. Nevertheless, the estimation accuracy will inevitably decrease, which leads to the fluctuation in Fig. 5(b).

The comparative experiment of the two methods leads to a conclusion that the PR-CPM method can realize the same performance as the PRPC method at much lower bandwidth requirement.

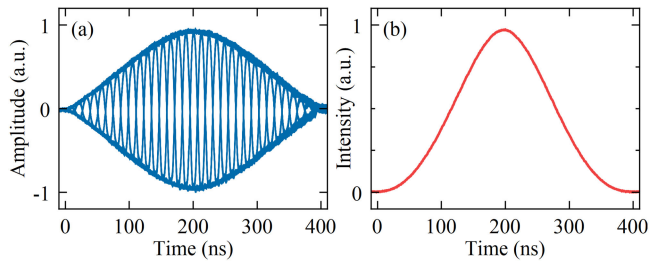


Fig. 7 (a) Eye diagram of the modulated lightwave with $T_b = 12$ ns in PR-CPM method. (b) The intensity envelope of the phase modulated pulse.

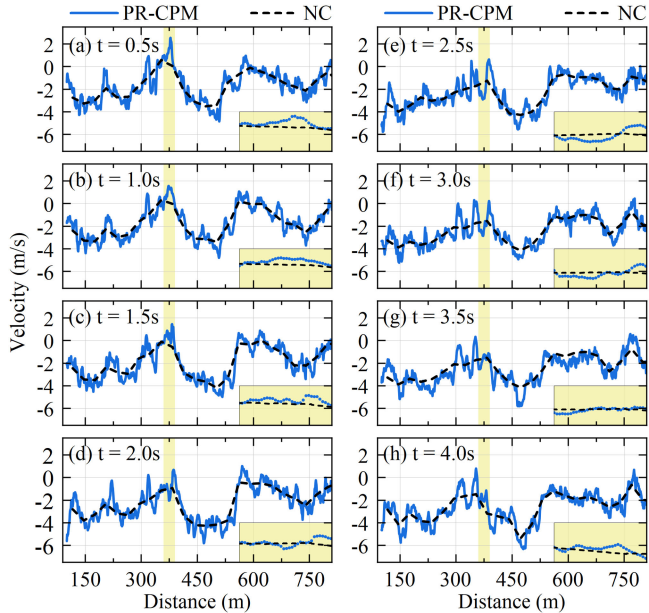


Fig. 8. Radial wind velocity profiles obtained by continuous observation of 4 s. Insert: Enlarged wind profiles from 360 to 390 m, where the span of the velocity axis is 8.5 m/s.

B. High-Spatial-Resolution Wind Profiling

To further demonstrate the performance of the PR-CPM method, a high-spatial-resolution experiment is carried out. The modulation bit interval is configured as 12 ns to realize the spatial resolution of 1.8 m. The eye diagram of the modulated lightwave in the CPM-12ns is shown in Fig. 7(a). Since the phase modulation doesn't affect the intensity, the modulated pulses share the same intensity envelope as shown in Fig. 7(b), where the FWHM of the intensity waveform is measured to be 170 ns. Meanwhile, to validate the measurement by the PR-CPM lidar, a conventional non-coding lidar with the same pulse intensity envelope is used as a reference, which would be referred to as NC-170ns. It should be noted that the current hardware described in Section III (mainly the AWG) cannot support the PRPC method working at such a high spatial resolution.

Fig. 8 shows the wind velocity profiles obtained by the two methods, where the blue solid line and black dash line stand for the CPM-12ns and NC-170ns, respectively. The evolution of the wind field is continuously profiled for 4 s with the

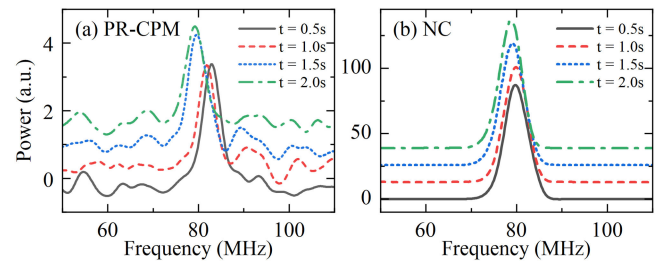


Fig. 9. Spectra continuously measured by the (a) CPM-12ns and (b) NC-170ns at 380 m.

spatial/temporal resolution of 1.8 m/0.5 s. The high spatial resolution wind profile CPM-12ns varies around the NC-170ns continuously over time. Differences between the two sets of profiles can be observed at some distances (like around 380 m, shaded by yellow in Fig. 8), which can be attributed to the spatial smoothing effect [43] caused by the low spatial resolution of the NC-170ns.

Fig. 9 shows the backscattered spectra at 380 m, where the curves corresponding to the spectra at different time are shifted in the y-axis for clarity. The spectra change continuously through time, which further suggests that the difference is more likely to be the time-varying characteristics of the fine wind field than the random measurement noise. The width of the main spectral peak in the CPM-12ns is close to the spectrum width of the NC-170ns, though the spatial resolution of the two method are quite different. The signal power of the NC-170ns is higher, as its low spatial resolution equivalently increases the diversity number [37].

V. CONCLUSION

A coherent Doppler wind lidar based on pseudo-random continuous phase modulation is proposed and experimentally demonstrated. With the help of the spectrum spreading property, the range resolved signals are separated through different time delays. By eliminating the abrupt phase switching between successive bit intervals, the new method provides higher modulation efficiency and avoids the degradations related to the non-instantaneous transition edges. In experiments, the performance of the proposed method is compared with the PRPC method at the same spatial resolution, showing a 10-fold modulation efficiency improvement. Continuous radial wind profile measurement of 800 m is demonstrated with spatial and temporal resolution of 1.8 m and 0.5 s, which is the highest spatial resolution realized by a pulsed CDWL to our best knowledge.

Considering that the phase modulation doesn't change the intensity envelope of pulses, the PR-CPM method is inherently compatible with the conventional pulsed CDWL. By upgrading the deployed systems, the proposed method is promising to provide a high-efficiency and low-cost remote sensing approach for areas like aviation safety and aerodynamic research.

REFERENCES

- [1] Z. Liu et al., "A review of progress and applications of pulsed doppler wind LiDARs," *Remote Sens.*, vol. 11, no. 21, Sep. 2019, Art. no. 2522.
- [2] B. Witschas, S. Rahm, A. Dörnbrack, J. Wagner, and M. Rapp, "Airborne wind lidar measurements of vertical and horizontal winds for the investigation of orographically induced gravity waves," *J. Atmos. Ocean. Technol.*, vol. 34, no. 6, pp. 1371–1386, Jun. 2017.
- [3] M. Jia et al., "Long-lived high-frequency gravity waves in the atmospheric boundary layer: Observations and simulations," *Atmos. Chem. Phys.*, vol. 19, no. 24, pp. 15431–15446, Dec. 2019.
- [4] Y. Yang et al., "Diurnal evolution of the wintertime boundary layer in Urban Beijing, China: Insights from doppler lidar and a 325-m meteorological tower," *Remote Sens.*, vol. 12, no. 23, Dec. 2020, Art. no. 3935.
- [5] S. H. Yim, "Development of a 3D real-time atmospheric monitoring system (3DREAMS) using Doppler LiDARs and applications for long-term analysis and hot-and-polluted episodes," *Remote Sens.*, vol. 12, no. 6, Mar. 2020, Art. no. 1036.
- [6] Y. Käsler, S. Rahm, R. Simmet, and M. Kühn, "Wake measurements of a multi-MW wind turbine with coherent long-range pulsed Doppler wind lidar," *J. Atmos. Ocean. Technol.*, vol. 27, no. 9, pp. 1529–1532, Sep. 2010.
- [7] M. A. Mohandes and S. Rehman, "Wind speed extrapolation using machine learning methods and LiDAR measurements," *IEEE Access*, vol. 6, pp. 77634–77642, 2018.
- [8] N. J. Harvey, R. J. Hogan, and H. F. Dacre, "Evaluation of boundary-layer type in a weather forecast model utilizing long-term Doppler lidar observations," *Quart. J. Roy. Meteorological Soc.*, vol. 141, no. 689, pp. 1345–1353, Apr. 2015.
- [9] M. Weissmann, R. H. Langland, C. Cardinali, P. M. Pauley, and S. Rahm, "Influence of airborne Doppler wind lidar profiles near Typhoon Sinlaku on ECMWF and NOGAPS forecasts," *Quart. J. Roy. Meteorological Soc.*, vol. 138, no. 662, pp. 118–130, Jan. 2012.
- [10] Y. Yang et al., "Characteristics of heavy particulate matter pollution events over Hong Kong and their relationships with vertical wind profiles using high-time-resolution Doppler lidar measurements," *J. Geophys. Res.: Atmos.*, vol. 124, no. 16, pp. 9609–9623, Dec. 2019.
- [11] M. Li, N. Fu, X. Xiong, and Y. Ma, "Novel method based upon combined lidar system for PM2.5 detection," *IEEE Photon. J.*, vol. 14, no. 1, Feb. 2022, Art. no. 6003508.
- [12] T. Wei, H. Xia, B. Yue, Y. Wu, and Q. Liu, "Remote sensing of raindrop size distribution using the coherent Doppler lidar," *Opt. Exp.*, vol. 29, no. 11, pp. 17246–17257, May 2021.
- [13] J. Yuan, H. Xia, T. Wei, L. Wang, B. Yue, and Y. Wu, "Identifying cloud, precipitation, windshear, and turbulence by deep analysis of the power spectrum of coherent Doppler wind lidar," *Opt. Exp.*, vol. 28, no. 25, pp. 37406–37418, Dec. 2020.
- [14] J. Yuan et al., "Cloud seeding evidenced by coherent Doppler wind lidar," *Remote Sens.*, vol. 13, no. 19, Sep. 2021, Art. no. 3815.
- [15] L. Thobois, J. P. Cariou, and I. Gultepe, "Review of lidar-based applications for aviation weather," *Pure Appl. Geophys.*, vol. 176, no. 5, pp. 1959–1976, May 2019.
- [16] J. Huang, M. K. P. Ng, and P. W. Chan, "Wind shear prediction from light detection and ranging data using machine learning methods," *Atmosphere*, vol. 12, no. 5, May 2021, Art. no. 644.
- [17] P. W. Chan, "LIDAR-based turbulence intensity calculation using glide-path scans of the Doppler Light detection and ranging (LIDAR) systems at the Hong Kong international airport and comparison with flight data and a turbulence alerting system," *Meteorologische Zeitschrift*, vol. 19, no. 6, pp. 549–563, Dec. 2010.
- [18] V. A. Banakh and I. N. Smalikho, "Lidar studies of wind turbulence in the stable atmospheric boundary layer," *Remote Sens.*, vol. 10, no. 8, Aug. 2018, Art. no. 1219.
- [19] I. N. Smalikho, V. A. Banakh, F. Holzäpfel, and S. Rahm, "Method of radial velocities for the estimation of aircraft wake vortex parameters from data measured by coherent Doppler lidar," *Opt. Exp.*, vol. 23, no. 19, pp. A1194–A1207, Sep. 2015.
- [20] I. N. Smalikho and V. A. Banakh, "Estimation of aircraft wake vortex parameters from data measured with a 1.5 μ m coherent Doppler lidar," *Opt. Lett.*, vol. 40, no. 14, pp. 3408–3411, Jul. 2015.
- [21] R. Solanki et al., "Elucidating the atmospheric boundary layer turbulence by combining UHF radar wind profiler and radiosonde measurements over urban area of Beijing," *Urban Climate*, vol. 43, May 2022, Art. no. 101151.
- [22] R. Torun, M. M. Bayer, I. U. Zaman, J. E. Velasco, and O. Boyraz, "Realization of multitone continuous wave LiDAR," *IEEE Photon. J.*, vol. 11, no. 4, Aug. 2019, Art. no. 5501910.
- [23] Z. Tang et al., "Source location and suppression of phase induced intensity noise in fiber-based continuous-wave coherent Doppler lidar," *IEEE Photon. J.*, vol. 13, no. 3, Jun. 2021, Art. no. 7200410.
- [24] C. F. Abari, A. T. Pedersen, E. Dellwik, and J. Mann, "Performance evaluation of an all-fiber image-reject homodyne coherent Doppler wind lidar," *Atmos. Meas. Tech.*, vol. 8, no. 10, pp. 4145–4153, Oct. 2015.
- [25] Y. Zhang, Y. Wu, and H. Xia, "Spatial resolution enhancement of coherent Doppler wind lidar using differential correlation pair technique," *Opt. Lett.*, vol. 46, no. 22, pp. 5550–5553, Nov. 2021.
- [26] C. Liang, C. Wang, X. Xue, X. Dou, and T. Chen, "Meter-scale and sub-second-resolution coherent Doppler wind LIDAR and hyperfine wind observation," *Opt. Lett.*, vol. 47, no. 13, pp. 3179–3182, Jul. 2022.
- [27] Y. Zhang, Y. Wu, and H. Xia, "Spatial resolution enhancement of coherent Doppler lidar by pseudo-random phase coding," *J. Lightw. Technol.*, vol. 40, no. 13, pp. 4467–4473, Jul. 2022.
- [28] J. G. Proakis and M. Salehi, "Digital modulation schemes," in *Digital Communications*, 5th ed., New York, NY, USA: McGraw-Hill Education, 2007.
- [29] D. A. Shaddock, "Digitally enhanced heterodyne interferometry," *Opt. Lett.*, vol. 32, no. 22, pp. 3355–3357, Nov. 2007.
- [30] J. G. Proakis and M. Salehi, "Digital communication through band-limited channels," in *Digital Communications*, 5th ed., New York, NY, USA: McGraw-Hill Education, 2007.
- [31] P. Salamitou, A. Dabas, and P. H. Flamant, "Simulation in the time domain for heterodyne coherent laser radar," *Appl. Opt.*, vol. 34, no. 3, pp. 499–506, Jan. 1995.
- [32] Q. Liu, X. Fan, and Z. He, "Time-gated digital optical frequency domain reflectometry with 1.6-m spatial resolution over entire 110-km range," *Opt. Exp.*, vol. 23, no. 20, pp. 25988–25995, Oct. 2015.
- [33] N. Riesen, T. T. Y. Lam, and J. H. Chow, "Bandwidth-division in digitally enhanced optical frequency domain reflectometry," *Opt. Exp.*, vol. 21, no. 4, pp. 4017–4026, Feb. 2013.
- [34] J. G. Proakis and M. Salehi, "Spread spectrum signals for digital communications," in *Digital Communications*, 5th ed., New York, NY, USA: McGraw-Hill Education, 2007.
- [35] Y. Jeong, J. K. Sahu, D. B. S. Soh, C. A. Codemard, and J. Nilsson, "High-power tunable single-frequency single-mode erbium:Ytterbium codoped large-core fiber master-oscillator power amplifier source," *Opt. Lett.*, vol. 30, no. 22, pp. 2997–2999, Nov. 2005.
- [36] J. G. Proakis and M. Salehi, "Optimum receivers for AWGN channels," in *Digital Communications*, 5th ed., New York, NY, USA: McGraw-Hill Education, 2007.
- [37] S. W. Henderson, P. Gatt, D. Rees, and R. M. Huffaker, "Wind lidar," in *Laser Remote Sensing*, T. Fujii and T. Fukuchi Eds., Boca Raton, FL, USA: CRC, 2005.
- [38] R. G. Frehlich and M. J. Yadlowsky, "Performance of mean-frequency estimators for Doppler radar and lidar," *J. Atmos. Ocean. Technol.*, vol. 11, no. 5, pp. 1217–1230, Oct. 1994.
- [39] K. Kikuchi, "Fundamentals of coherent optical fiber communications," *J. Lightw. Technol.*, vol. 34, no. 1, pp. 157–179, Jan. 2016.
- [40] H. W. Johnson and M. Graham, *High-Speed Digital Design: A Handbook of Black Magic*. Englewood Cliffs, NJ, USA: Prentice Hall, 1993.
- [41] S. W. Henderson, P. Gatt, D. Rees, and R. M. Huffaker, "Wind lidar," in *Laser Remote Sensing*, T. Fujii and T. Fukuchi Eds. Boca Raton, FL, USA: CRC, 2005, pp. 520–523, ch. 7.
- [42] B. J. Rye and R. M. Hardesty, "Discrete spectral peak estimation in incoherent backscatter heterodyne lidar. I. Spectral accumulation and the Cramer-Rao lower bound," *IEEE Geosci. Remote Sens. Lett.*, vol. 31, no. 1, pp. 16–27, Jan. 1993.
- [43] S. Zaslowski, Z. Yang, and L. Thévenaz, "On the 2D post-processing of Brillouin optical time-domain analysis," *J. Lightw. Technol.*, vol. 38, no. 14, pp. 3723–3736, Jul. 2020.